ELSEVIER

Physics of the Earth and Planetary Interiors 119 (2000) 57–74

PHYSICS
OF THE EARTH
AND PLANETARY
INTERIORS

www.elsevier.com/locate/pepi

Effect of a plume on long period surface waves computed with normal modes coupling

Yann Capdeville *, Eléonore Stutzmann, Jean Paul Montagner

Département de Sismologie, URA 195, Institut de Physique du Globe de Paris, 4 Place Jussieu, 75252 Paris, France

Received 1 December 1997; received in revised form 23 November 1998; accepted 2 December 1998

Abstract

The physical characterization and depth origin of mantle plumes are not well constrained. In order to address these issues, we look for observable effects of plumes on long period surface wave seismograms. The effect of a weak but sharp heterogeneity on long period surface waves is computed by a first order normal mode theory using a generalization of the spherical harmonic summation theorem to reduce the number of operations. It turns out that it is necessary to couple very far along a given dispersion branch ($l \pm 40$ up to ± 80) to remove spurious phases in seismograms. The coupling between different overtone branches (different overtone numbers) of the same kind (spheroidal or toroidal) and of different kinds are computed as well. By taking into account a large number of overtones, we are able to compute the effect of the heterogeneity on all seismogram phases from surface waves to body waves, including P–SH and SV–SH coupling. This technique is applied to different plausible models of mantle plume: a small vertical conduit down to 660 km depth, down to the core–mantle-boundary (CMB) and with or without head. We show that for a finite size plume the radiation pattern is essentially forward, which is not the case when the heterogeneity is considered as punctual. The scattered amplitude displays large variations for the different cases according to the temperature contrast, but an effect up to 10% of the incident amplitude can be expected, and should be observable on good quality seismic data.

Keywords: Surface waves; Normal modes; Born approximation; Hotspot

1. Introduction

Oceanic islands often form long lines of volcanoes of progressively increasing ages, suggesting that they have been created by stationary heat sources under moving tectonic plates. Morgan (1971) named this kind of volcanoes hotspots and first suggested that these heat sources could be related to mantle plumes rising from deep in the mantle. Thanks to their assumed stationarity, plumes have been extensively used as a reference frame to determine absolute plate motions (Minster and Jordan, 1978).

In order to verify the hypothesis of Morgan (1971) and to get more information on the physical properties of plumes, geochemical, fluid dynamical and seismological studies have been performed. Geochemists have found some evidences that basalts of some of these intra-plate volcanoes have a deep mantle origin (see, for example, Hart et al. (1992) or

---

* Corresponding author. Tel.: +33-1-44272469; fax: +33-1-44273894; e-mail: capdevil@ipgp.jussieu.fr

PII: S0031-9201(99)00153-3

Hofmann (1997)). Fluid dynamic studies have shown that plumes should originate from instabilities in thermal boundary layers, such as the D″ layer (Stacey and Loper, 1983) or the mantle transition zone. Fluid dynamic experiments (Whitehead and Luther, 1975; Griffiths and Campell, 1990) and fluid dynamics modeling (Olson et al., 1987; Farnetani and Richards, 1995) show that a plume consists of a large head followed by a thin tail. From the point of view of seismology, some global and regional studies have been performed. At a global scale, the hotspot distribution has been compared with the lateral heterogeneities of tomographic models. Cazenave et al. (1989) and Montagner and Romanowicz (1993) have found some good correlations between 2° and 6° of the spherical harmonic expansion of the hotspot distribution and the lateral heterogeneities of tomographic models. There might be two families of plumes, the first one originating in the D″ and the second one in the transition zone (Montagner, 1994). Global tomography models also show low velocity anomalies under some hotspots (see for example Zhang and Tanimoto, 1993; Trampert and Woodhouse, 1995; Grand et al., 1997; Van Der Hilst et al., 1997), but they are not stable from one model to the other. Indeed, plumes are probably very small, their lateral extent is by far smaller than the actual global tomography resolution. Therefore, this technique cannot provide strong constraints on the structure of plumes. Regional tomographic models also show low velocity anomalies under some hotspots (see, for example, Roult et al. (1994) or Silveira et al. (1998)). Regional seismological studies of plumes, and especially body wave studies, have also been performed: Nataf and Vandecar (1993) found small P wave time delays which were attributed to the Bowie plume at 700 km depth. Wolfe et al. (1997) found a cylindrical low velocity zone beneath Iceland down to 400 km depth with regional tomography. Vinnik et al. (1997) found evidences for a stagnant plume at the bottom of the transition zone, using P to S converted waves below stations of the central Pacific Ocean.

However, in spite of all this work, many questions are still pending: Are plumes really stationary? What is the exact shape of the tail, its radius, its bend, its depth origin and temperature contrast? Have they a head or not? What is their exact localization? etc...

The difficulty of the task is due to the probably small lateral extent of a plume, which implies a very small time delay of body waves and only a slight variation of the phase of surface waves. The small lateral extent of the plume compared to the wavelength gives rise to a scattering effect which could be exploited to retrieve the plume structure. This approach of scattering tomography has been followed for body waves to study plume structures in the lower mantle (Ying, 1996; Ying and Nataf, 1998) but without leading to a clear positive conclusion.

To a first approximation, a plume can be seen as a vertical cylinder of low seismic velocity. In a flat layered Earth, the effect of a cylindrical inclusion with constant velocity contrast has been studied by Bostock (1991) or Stange and Friederich (1992), both with a technique which allows to compute the complete wave field whatever the amplitude of the velocity contrast. Since we want to study the effect of some different shapes of a plume and temperature profiles, including the effect of Earth's sphericity, these two approaches are not suitable for our study. In this paper, we use the Born approximation in the framework of normal mode theory to study scattering effect of surface waves due to heterogeneities of small lateral extent. After some theoretical considerations on mode coupling, the scattering effects of the different plume geometries are quantified. The optimum geometrical configuration between earthquakes, plume and stations to observe the signal scattered from the plume in data is also discussed.

2. Theory

Since plumes are supposed to be a weak heterogeneity of density and elastic parameters, a first order perturbation theory can be used depending on the ratio of the radius of the plume versus the shortest wavelength of the incident signal. The perturbation of long period surface waves due to any weak heterogeneity, which maximum size will be discussed later, can be computed by using the Born approximation in the framework of the normal mode theory (see, for example, Tanimoto (1984a) or Clévédé and Logonné (1996)). We apply this theory to a sharp heterogeneity such as a plume.

The equation of motion in an SNRA (Spherical Non-Rotating Anelastic) Earth model can be written,

$$\rho_0 \partial_t^2 \mathbf{u}(t) + A\mathbf{u}(t) = \mathbf{f}(t), \tag{1}$$

where $\mathbf{u}(t)$ is the displacement field, ρ_0 the Earth's density, A the anelasto-dynamic operator and $\mathbf{f}$ the body force representing the earthquake source. In the Fourier–Laplace space and using the Quantum Mechanics formalism (Cohen-Tannoudji et al., 1977; see, for example, Malischewsky (1987) or Montagner (1996) for its application to seismology), this equation can be rewritten:

$$\overline{H}|\bar{\mathbf{u}}\rangle = |\bar{\mathbf{f}}\rangle, \tag{2}$$

with $\overline{H} = -P\sigma^2 + A$, where $P = \rho_0 I$, I the identity operator, σ the complex frequency and the Fourier–Laplace transform is defined as follows:

$$|\bar{\mathbf{u}}(\sigma)\rangle = \int_0^{+\infty} |\mathbf{u}(t)\rangle \mathrm{e}^{-i\sigma t}\mathrm{d}t. \tag{3}$$

Let us also define:

$$\langle \mathbf{u}|B|\mathbf{v}\rangle = \int_E \mathbf{u}^* . B(\mathbf{v})\mathrm{d}V, \tag{4}$$

for any operator B, where E is the Earth's volume, asterisk denotes complex conjugation and dot the dot product.

We assume that the set $\{|\mathbf{u}_k\rangle\}$ of eigenvectors that solves:

$$A|\mathbf{u}_k\rangle = \rho_0 \sigma_k^2 |\mathbf{u}_k\rangle, \tag{5}$$

forms a complete basis of functions for the displacement space of the Earth. These eigenvectors only depend on four integers, s, n, l and m, and are denoted $|\mathbf{u}_k\rangle = |\mathbf{k}\rangle \mathrm{e}^{i\sigma_k t}$ with $|\mathbf{k}\rangle = |s, n, l, m\rangle$. The index s indicates a toroidal or a spheroidal mode, n is the overtone number, l the angular degree and m the azimuthal order. These eigenvectors are assumed to be equal to those computed in the elastic case, but they are associated with the complex frequency $\sigma_k = \omega_k(1 + i/2Q_k)$, where ω_k is the eigenfrequency in the elastic case, Q_k the quality factor of the mode k, which is a good approximation of the anelastic case (Clévédé, 1991). We have then:

$$|\mathbf{k}\rangle = {}_n\mathbf{D}_l Y_l^m(\theta,\phi) \tag{6}$$

where ${}_n\mathbf{D}_l$ is the displacement operator:

$${}_n\mathbf{D}_l = {}_nU_l(r)\mathbf{r} + {}_nV_l(r)\nabla_1 + {}_nW_l(r)(-\mathbf{r}\times\nabla_1), \tag{7}$$

where ${}_nU_l$, ${}_nV_l$ and ${}_nW_l$ are the radial eigenfunctions, ${}_nU_l = {}_nV_l = 0$ for a toroidal mode and ${}_nW_l = 0$ for a spheroidal one, Y_l^m are the spherical harmonics and ∇_1 the surface gradient operator on the unit sphere. Modes are normalized according to $\langle \mathbf{k}|\rho_0|\mathbf{k}'\rangle = \delta_{kk'}$, ($\delta_{kk'}$ is the Kronecker symbol), which can be written for $k = k'$, by separating toroidal and spheroidal modes,

$$\begin{aligned}&\int_0^a \rho_0\big({}_nU_l^2(r) + l(l+1){}_nV_l^2(r)\big)r^2\mathrm{d}r\\ &\quad= \int_0^a \rho_0 l(l+1){}_nW_l^2(r)r^2\mathrm{d}r = 1,\end{aligned} \tag{8}$$

where a is Earth's radius.

A slight perturbation of the density and the elastic moduli of the reference model is now considered. The operator $\overline{H}$ then becomes $\overline{H} + \delta\overline{H}$ where $\delta\overline{H} = \delta A - \sigma^2\delta P$, and the SNRAI seismogram $\mathbf{u}$ becomes $\mathbf{u} + \delta\mathbf{u}$, where $\delta\mathbf{u}$ is the perturbation to $\mathbf{u}$ due to the heterogeneity. Therefore Eq. (2) is rewritten:

$$(\overline{H} + \delta\overline{H})(|\bar{\mathbf{u}}\rangle + |\delta\bar{\mathbf{u}}\rangle) = |\bar{\mathbf{f}}\rangle. \tag{9}$$

To first order, the expression of $\delta\bar{\mathbf{u}}$ is:

$$|\delta\bar{\mathbf{u}}\rangle = -\overline{H}^{-1}\delta\overline{H}\,\overline{H}^{-1}|\bar{\mathbf{f}}\rangle. \tag{10}$$

Since the basis of the normal mode eigenfunctions is assumed to be complete, $|\delta\bar{\mathbf{u}}\rangle$ can be expanded on this basis as follows:

$$|\delta\bar{\mathbf{u}}\rangle = \sum_k \delta\bar{a}_k(\sigma)|\mathbf{k}\rangle, \tag{11}$$

where $\delta\bar{a}_k(t)$ are the excitation coefficients of $|\delta\bar{\mathbf{u}}\rangle$. Projecting Eq. (11) on $\langle\mathbf{k}|\rho_0$, we obtain:

$$\begin{aligned}\delta\bar{a}_k &= \langle\mathbf{k}|\rho_0|\delta\bar{\mathbf{u}}\rangle,\\ \delta\bar{a}_k &= -\langle\mathbf{k}|\rho_0\overline{H}^{-1}\delta\overline{H}\,\overline{H}^{-1}|\bar{\mathbf{f}}\rangle,\end{aligned} \tag{12}$$

and, by using the closure relation $I = \sum_k \rho_0|\mathbf{k}\rangle\langle\mathbf{k}|$, where I is the identity operator:

$$\begin{aligned}\delta\bar{a}_k = -&\sum_{k'k''k'''}\langle\mathbf{k}|\rho_0^2\overline{H}^{-1}|\mathbf{k}''\rangle\langle\mathbf{k}''|\delta\overline{H}|\mathbf{k}'\rangle\\ &\times\langle\mathbf{k}'|\rho_0^2\overline{H}^{-1}|\mathbf{k}'''\rangle\langle\mathbf{k}'''|\bar{\mathbf{f}}\rangle.\end{aligned} \tag{13}$$

Since physical dispersion and the Earth's rotation are neglected, the expression of the matrix elements of $\rho_0^2\bar{H}^{-1}$ is (see Appendix A):

$$\left(\rho_0^2\bar{H}^{-1}\right)_{kk'} = \langle\mathbf{k}|\,\rho_0^2\bar{H}^{-1}|\mathbf{k}'\rangle = \delta_{kk'}/\left(\sigma_k^2-\sigma^2\right), \tag{14}$$

which leads to:

$$\delta\bar{a}_k = -\sum_{k'}\frac{\langle\mathbf{k}|\delta\bar{H}|\mathbf{k}'\rangle\langle\mathbf{k}'|\bar{\mathbf{f}}\rangle}{\left(\sigma_k^2-\sigma^2\right)\left(\sigma_{k'}^2-\sigma^2\right)}. \tag{15}$$

If a causal point source function, located in $\mathbf{r}_s$, $\mathbf{f}(\mathbf{r},t) = \mathbf{f}_0\delta(\mathbf{r}-\mathbf{r}_s)H(t)$ is assumed (here $H(t)$ is the Heaviside function) the expression of the total displacement, turning back to the time domain, ruling out the static terms and separating the summation over m from the other quantum numbers, is (Tanimoto, 1984a),

$$\begin{aligned}
\mathbf{v}.\mathbf{u} = \sum_K \Bigg\{ & -\frac{\cos(\sigma_K t)}{\sigma_K^2}\sum_m R_K^m S_K^m && (16.a)\\
& +\frac{\cos(\sigma_K t)}{\sigma_K^4}\sum_{mm'} R_K^m S_K^{m'}\delta A_{KK}^{mm'} + \frac{t\sin(\sigma_K t)}{2\sigma_K^3}\\
& \times\sum_{mm'} R_K^m\left(\delta A_{KK}^{m'm} - \sigma_K^2\delta P_{KK}^{m'm}\right)S_K^{m'} && (16.b)\\
& +\sum_{K'\neq K}\Bigg(\frac{\cos(\sigma_K t)}{\left(\sigma_{K'}^2-\sigma_K^2\right)\sigma_K^2}\\
& \times\sum_{mm'} R_K^m S_{K'}^{m'}\left(\delta A_{KK'}^{mm'} - \sigma_K^2\delta P_{KK'}^{mm'}\right)\Bigg) && (16.c)\\
& +\sum_{K'\neq K}\Bigg(\frac{\cos(\sigma_{K'} t)}{\left(\sigma_K^2-\sigma_{K'}^2\right)\sigma_{K'}^2}\\
& \times\sum_{mm'} R_K^m S_{K'}^{m'}\left(\delta A_{KK'}^{mm'} - \sigma_{K'}^2\delta P_{KK'}^{mm'}\right)\Bigg)\Bigg\}. && (16.d)
\end{aligned}$$

where $K=(s,n,l)$, $\mathbf{r}_r$ and $\mathbf{r}_s$ are, respectively, the receiver and source locations, $\mathbf{v} = \mathbf{v}_0\delta(\mathbf{r}-\mathbf{r}_r)$, $\mathbf{v}_0$ is the orientation of the receiver (the instrument response can be included in $\mathbf{v}$ if necessary) and:

$$\begin{aligned}
& R_k(\mathbf{r}_r) = \langle\mathbf{v}|\mathbf{k}\rangle,\\
& S_k(\mathbf{r}_s) = \langle\mathbf{k}|\mathbf{f}\rangle,\\
& \delta A_{kk'} = \langle\mathbf{k}|\delta A|\mathbf{k}'\rangle,\\
& \delta P_{kk'} = \langle\mathbf{k}|\delta P|\mathbf{k}'\rangle.
\end{aligned} \tag{17}$$

Eq. (16.a) corresponds to the classical expression of the unperturbed seismogram, Eq. (16.b) corresponds to the interaction between singlets of the same multiplet ($s=s'$, $n=n'$, $l=l'$, summation only over m and m'). Eqs. (16.c) and (16.d) correspond to the coupling between the different multiplets ($s\neq s'$ or $n\neq n'$ or $l\neq l'$). The summations over n, n', l and l' should take values from 0 to $+\infty$, the summations over m and m' from $-l$ to $+l$ and $-l'$ to $+l'$, respectively. The indices s and s' correspond either to toroidal modes and to spheroidal modes.

Eq. (16.b), normalized by the unperturbed term $\sigma_K^{-2}\sum_m R_K^m S_K^m$, includes a secular term in $t\varepsilon$, with:

$$\varepsilon = \frac{\sum_{mm'} R_K^m\delta H_K^{m'm}S_K^{m'}}{2\sigma_K\sum_m R_K^m S_K^m}.$$

This secular term appears when both eigenfunctions are degenerate ($s=s'$, $n=n'$, $l=l'$, $m\neq m'$). Therefore, expression (16a–d) is only valid for ''short'' times such as $t\varepsilon\ll 1$. In our application of a plume heterogeneity, ε never exceeds 10^{-5} s^{-1}, we can then consider that ''short time'' is met for $t<10^4$ s. Since we are only interested in scattered signal of the direct wave train (R1), this condition is always met.

We now need to compute the vectors and the matrices present in Eq. (17), particularly $\delta A_{kk'}$ and $\delta P_{kk'}$. When considering large scale heterogeneity, these splitting matrices are usually computed by expanding the perturbation of the elastic parameters and the density into spherical harmonics (see for example Woodhouse and Dahlen, 1978; Woodhouse and Girnius, 1982; Tanimoto, 1984b). When a small structure is considered, it would be necessary to expand the heterogeneity up to a very high degree of spherical harmonics, making the numerical problem very heavy. We prefer the approach in terms of point scatterers, represented by delta functions, more general than the one used by Snieder (1986a), Snieder and Nolet (1987) or Romanowicz (1987), both valid in the asymptotic surface wave formalism case.

The splitting matrix elements expression is:

$$\delta A_{kk'} = \langle k|\delta A|k'\rangle = \int_E \mathbf{u}_k(\mathbf{r})^*.\delta A\left(\mathbf{u}_{k'}(\mathbf{r})\right)\mathrm{d}\mathbf{r}, \tag{18}$$

where E is the Earth's volume and k denotes the pair (K,m). If the volume integration over the Earth is done numerically, Eq. (18) becomes:

$$\begin{aligned}\delta A_{kk'} &\simeq \sum_{d=1}^{n_d} \mathbf{u}_k(\mathbf{r}_d)^* . \delta A(\mathbf{u}_{k'}(\mathbf{r}_d)) \mathrm{d}V_d \\ &= \sum_d \delta A_{kk'}(\mathbf{r}_d), \end{aligned} \tag{19}$$

where $\{\mathbf{r}_d\}$ are the n_d numerical integration points and $\mathrm{d}V_d$ their corresponding volume element. $\delta A_{kk'}(\mathbf{r}_d)$ is the splitting matrix due to the following point heterogeneity located at $\mathbf{r}_d$:

$$\mathrm{d}V_d \delta\mu(\mathbf{r}_d)\delta(\mathbf{r}-\mathbf{r}_d), \quad \mathrm{d}V_d \delta\lambda(\mathbf{r}_d)\delta(\mathbf{r}-\mathbf{r}_d). \tag{20}$$

$\delta P_{kk'}(\mathbf{r}_d)$, due to

$$\mathrm{d}V_d \delta\rho(\mathbf{r}_d)\delta(\mathbf{r}-\mathbf{r}_d), \tag{21}$$

is similarly defined, where $\delta\rho(\mathbf{r}_d)/\rho_0$, $\delta\mu(\mathbf{r}_d)/\mu_0$ and $\delta\lambda(\mathbf{r}_d)/\lambda_0$ are very small compared to 1. Therefore, the splitting matrix due to a complex structure is only a finite sum of the splitting matrices due to a point scatterer with the appropriate weight.

The vectors R_k and S_k, and the matrices $\delta A_{kk'}(\mathbf{r}_d)$ and $\delta P_{kk'}(\mathbf{r}_d)$, are decomposed into the generalized spherical harmonics basis (Phinney and Burridge, 1973), using the notation of Woodhouse and Girnius (1982):

$$R_k(r_r,\theta_r,\phi_r) = \sum_{N=-1}^{N=1} R_{KN}(r_r) Y_l^{Nm}(\theta_r,\phi_r), \tag{22}$$

$$S_k(r_s,\theta_s,\phi_s) = \sum_{N=-2}^{N=2} S_{KN}(r_s) Y_l^{Nm*}(\theta_s,\phi_s), \tag{23}$$

$$\begin{aligned}&\delta A_{kk'}(r_d,\theta_d,\phi_d) \\ &\quad = \sum_{N=-2}^{N=2} \delta A_{KK'N}(r_d) Y_l^{Nm*}(\theta_d,\phi_d) Y_{l'}^{Nm'}(\theta_d,\phi_d),\end{aligned} \tag{24}$$

$$\begin{aligned}&\delta P_{kk'}(r_d,\theta_d,\phi_d) \\ &\quad = \sum_{N=-2}^{N=2} \delta P_{KK'N}(r_d) Y_l^{Nm*}(\theta_d,\phi_d) Y_{l'}^{Nm'}(\theta_d,\phi_d),\end{aligned} \tag{25}$$

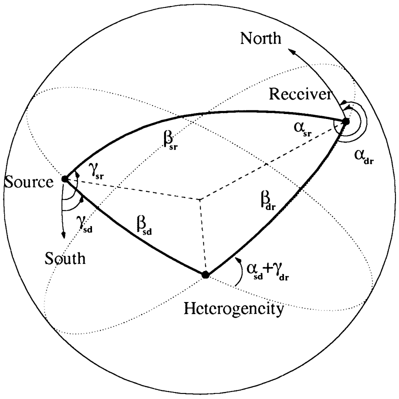

Fig. 1. Different angles used in this paper. All of them are measured anti-clockwise. β_{xy} is the angular distance between x and y (x and y stand for s, r and d), $\pi-\gamma_{sd}$ is the azimuth at the source between the source and the heterogeneity, $\alpha_{sd}+\gamma_{dr}$ is the scattering angle and $-\alpha_{dr}$ is the back-azimuth at the receiver between the heterogeneity and the receiver.

where $(r_d,\theta_d,\phi_d) = \mathbf{r}_d$ are the coordinates of the numerical integration points, which can be regarded as point scatterers.

The expressions of R_{KN} and S_{KN} are given by Woodhouse and Girnius (1982), $\delta A_{KK'N}$ and $\delta P_{KK'N}$ are given in Appendix B. Since the calculation of $\sum_{mm'} R_K^m S_{K'}^{m'} \delta H_{KK'}^{mm'}$ becomes more and more time consuming with increasing l, it is expedient to use a generalization of the classical summation theorem, valid for the generalized spherical harmonics (Edmonds, 1960; Li and Tanimoto, 1993):

$$\begin{aligned}&\sum_{m=-l}^{m=l} Y_l^{N'm*}(\theta_s,\phi_s) Y_l^{Nm}(\theta_r,\phi_r) \\ &\quad = \mathrm{e}^{iN'\gamma_{sr}} P_l^{NN'}(\cos(\beta_{sr})) \mathrm{e}^{iN\alpha_{sr}},\end{aligned} \tag{26}$$

where $P_l^{NN'}$ are the generalized Legendre functions. If the index s is related to the source location and r to the receiver one, then the angle $-\alpha_{sr}$ is the back-azimuth at the receiver, $\pi-\gamma_{sr}$ the azimuth at the source and β_{sr} is the angular epicentral distance (see Fig. 1). This leads to:

$$\begin{aligned}&\sum_{mm'} R_K^m S_{K'}^{m'} \delta H_{KK'}^{mm'} \\ &\quad = \sum_{NN'N''} \Big(R_{KN} \mathrm{e}^{iN\alpha_{dr}} S_{K'N'} \mathrm{e}^{iN'\gamma_{sd}} \\ &\quad \times \delta H_{KK'N''} \mathrm{e}^{iN''(\gamma_{dr}+\alpha_{sd})} . P_{l'}^{N''N'}(\cos(\beta_{sd})) \\ &\quad \times P_l^{NN''}(\cos(\beta_{dr})) \Big),\end{aligned} \tag{27}$$

where $\delta H_{KK'N''} = \delta A_{KK'N''} - \sigma_K^2 \delta P_{KK'N''}$, β_{xy} is the angular distance between x and y (x and y stand for s, r and d), $\pi - \gamma_{sd}$ is the azimuth at the source between the source and the heterogeneity, $\alpha_{sd} + \gamma_{dr}$ is the scattering angle and $-\alpha_{dr}$ is the back-azimuth at the receiver between the heterogeneity and the receiver (see Fig. 1). This simplification is numerically very important, since it avoids a number of operations increasing with l^2 (for example for $l = 250$ it will change $(2l+1)^2 = 251\,001$ operations into $N \cdot N' \cdot N'' = 75$ operations).

However, due to limitations in computation time, we cannot compute all interaction terms present in Eqs. (16.a), (16.b), (16.c) and (16.d), and therefore we have to apply different levels of approximations that are considered in Section 3.

3. Approximations in mode coupling

We first consider a very simple structure of a plume, named ''line plume'': a radial cylindrical heterogeneity of 100 km radius rising from the CMB, at 2900 km depth up to the surface. The cylinder is represented by a line of point heterogeneities. This approximation is valid for very long periods, when the lateral extent of the plume is assumed to be very small compared to the wavelength. The error resulting from this approximation will be considered in Section 4.

We consider several types of approximation in evaluating Eqs. (16.a), (16.b), (16.c) and (16.d), listed below in order of increasing accuracy:

- The coupling within multiplets is performed according to Eq. (16.b), which corresponds to the ''isolated multiplet'' approximation, i.e., the lowest level of approximation.
- Then interactions between multiplets along a given branch ($n = n'$ fixed and $l \neq l'$ varying) can be taken into account by including Eqs. (16.c) and (16.d) in the computation.
- Finally, complete interactions among modes of the same kind s and between spheroidal and toroidal modes ($s \neq s'$) is computed with Eqs. (16.c) and (16.d) (by varying n and l).

These different levels of approximation are successively considered in this section and we show their effect on synthetic seismograms.

3.1. Isolated multiplet approximation

Let us start with the ''isolated multiplet'' approximation: only Eq. (16.b) is computed for each (s, n, l). The vertical seismogram in Fig. 2b is computed for PREM reference Earth model (Dziewonski and Anderson, 1981) and only the first three trains R1, R2 and R3 are displayed. It is computed for a vertical normal fault source and a receiver both located on the equator with an epicentral distance of 60°, and only the fundamental mode has been taken into account. Fig. 2c shows the scattered seismogram

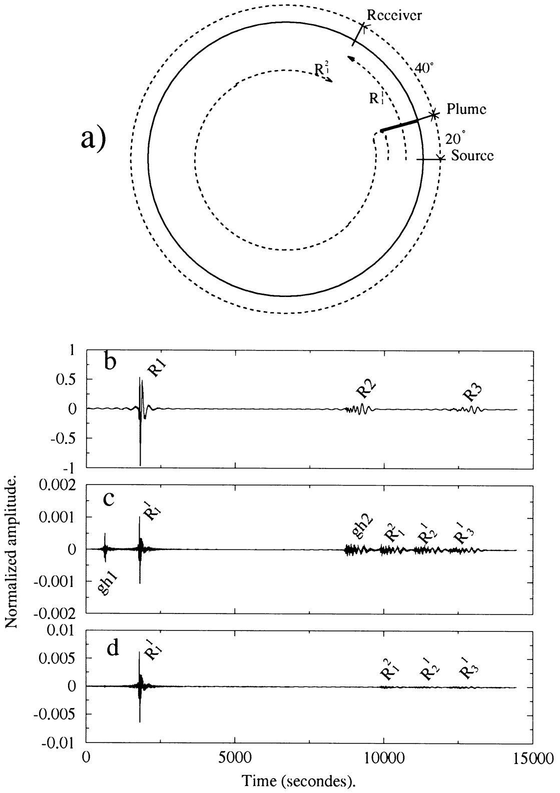

Fig. 2. (a) Source, receiver and plume location. The path of the minor arc scattered train of R1, R_1^1, and the path of major arc scattered train of R1, R_1^2, are also displayed. (b) Fundamental mode seismogram for the reference Earth model (PREM). (c) Scattered seismogram due to ''line plume'' (see Section 3) computed in the isolated multiplet approximation. $gh1$ and $gh2$ are ghost trains. (d) Scattered seismogram by taking into account the coupling along the dispersion branch $n = 0$. In that case ''ghost'' trains vanish. The minimum period used here is 25 s ($l_{\max} = 415$), and tapering in the frequency domain has been used.

computed for the isolated multiplet approximation (Eq. (16.b)) generated by a ''line plume'' of -10% of $\delta\lambda$, located on the source receiver minor arc at 20° from the source (see Fig. 2a). Only λ have been perturbed for sake of simplicity (see Appendix C), but the same conclusion would raise with μ or ρ. In the case of a sharp and small heterogeneity, this approximation creates some artificial trains, named ''ghost'' trains, and a wrong amplitude. An example of such an effect is shown in Fig. 2b, where six trains can be seen. The first one ($gh1$) is clearly a ''ghost'' since it arrives before the R1 train. The forward effect of R1 arrives at the same time as R1, this is R_1^1 in Fig. 2c, the backward effect of R1, R_1^2, has to travel 340° so it roughly arrives at $t = 9800$ s, (assuming an approximated group velocity of 4 km s^{-1}). The backward effect of R2, R_2^2, has to travel 380° and it roughly arrives at $t = 10\,900$ s. The last train, R_3^1 is the forward effect of R3. $gh2$ and the first acausal train $gh1$ are not physical, that is the reason why we name them ''ghosts''. They always occur in the isolated multiplet approximation for any kind of heterogeneity. Ghosts are shown up in terms of propagating surface waves by using asymptotic expressions of Legendre functions and Poisson summation formula in Appendix C. A physical interpretation is that in the isolated multiplet approximation, only the even part of the structure is taken into account, and since a point heterogeneity is clearly not an even structure, it creates spurious trains. A plume located on the opposite side of the Earth would create scattered trains whose traveltime would fit ghosts traveltime except for the acausal one.

3.2. Coupling between multiplets along the same branch

To avoid these ghosts, it is absolutely necessary to couple different multiplets along the same dispersion branch, using Eqs. (16.c) and (16.d) as shown in Fig. 2d (a similar result is obtained in the case of a slab structure by Lognonné and Clévédé, 1997). It is not really surprising since coupling exists up to $\Delta l = s_{\max}$, where Δl is an integer such that all multiplets l and l' with $|l - l'| \leq \Delta l$ are coupled and $s_{\max}$ is the highest degree of the spherical harmonic expansion of the heterogeneity. In the case of a point heterogeneity $s_{\max} = \infty$, then we should theoretically couple up to infinity. From a practical point of view, we need to find the smallest Δl as possible to obtain an acceptable ghost amplitude. But, for a given Δl, if the accuracy of a perturbed seismogram is defined as the ratio of the ghost maximum amplitude versus the amplitude of the largest real scattered train, this accuracy widely varies according to the source-heterogeneity and heterogeneity-receiver distances. If they are far from each other, i.e., at least 20°, the decreasing of ghost amplitude towards zero is fast up to $\Delta l = 12$, but slow and oscillating later on. In this case, a good compromise between accuracy and

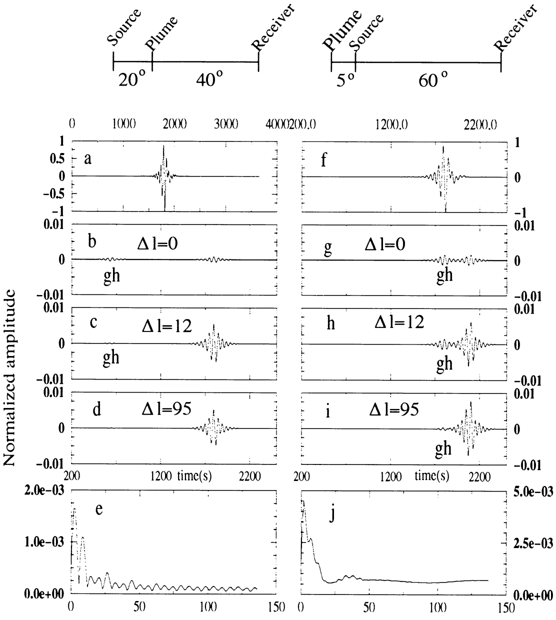

Fig. 3. Top: Source, receiver and heterogeneity (a ''line plume'' depicted in Section 3) configuration for left and right panels. In the left panels, the heterogeneity is located on the source receiver minor arc at 20° from the source. In the right panels, the heterogeneity is located on the source receiver major arc at 5° from the source. (a and f) Vertical component of the incident signal computed with fundamental mode for the reference Earth model for both configurations. (b and g) Vertical component of the scattered signal computed in the isolated multiplet approximation ($\Delta l = 0$). (c and h) Vertical component of the scattered signal computed coupling along the fundamental branch with $\Delta l = 12$. (d and i) Vertical component of the scattered computed coupling along the fundamental branch with $\Delta l = 95$. (e and j) Maximum amplitude of the ghost as a function of Δl for both configurations. The minimum period used here is 40 s ($l_{\max} = 254$), and tapering in the frequency domain has been used.

numerical effort is found for $\Delta l = 12$. On the other hand, if the receiver or the source is very close (1° or 2°) to the plume, it is necessary to couple multiplets at least up to $\Delta l = 90$.

This is illustrated in Fig. 3 for a line plume of -10% in λ (we would have to obtain similar results for ρ and μ) and for two different source, receiver and plume locations. In the left panels, source and station are far from each other while in the right panels, the plume is located at five degrees away from the source (see Fig. 3). Panels (a) and (f) show the vertical component of the incident signal for the fundamental mode. Panels (b,g), (c,h) and (d,i) display the perturbation due to the plume, by coupling along the fundamental branch for $\Delta l = 0$, $\Delta l = 12$ and $\Delta l = 95$, respectively. The two panels at the bottom, (e) and (j), present the amplitude of the ghost train as a function of Δl. Fig. 3e shows a fast decrease of the ghost amplitude, and then oscillations for large Δl. On the other hand, plot (j) shows a slower decrease of the ghost amplitude towards zero with increasing Δl.

Coupling up to $\Delta l = 100$ is not a numerical problem for a point heterogeneity, for the fundamental mode and without coupling between spheroidal and toroidal modes. However, it becomes a time consuming task in a more general case (i.e., when coupling a large number of higher modes and when taking into account the lateral extent of the plume by numerical integration, involving a large number of scattering points).

3.3. Coupling between multiplets from different branches

We proceed by considering the coupling of multiplets from different branches (cross-branch coupling). Since there is no theoretical difference between coupling of different multiplets from the same branch or from different branches, we use Eqs. (16.c) and (16.d), as in Section 3.2. From a practical point of view, it is necessary to be very careful because some eigenfrequencies are so close to each other that they have to be considered as degenerate in order to avoid numerical problems. It can easily be shown that when $\delta\omega_{KK'} = |\omega_K - \omega_{K'}|$ is becoming close to zero, Eqs. (16.c) and (16.d) are converging towards the isolated multiplet expression Eq. (16.b) as $t\delta\omega_{KK'}$. This is a short time approximation, such as the secular term of Eqs. (16.a), (16.b), (16.c) and (16.d). Two multiplets are named ‘‘quasi degenerated’’ if the error due to this approximation is the same as the one due to the secular term (in practice $\delta\omega_{KK'} < 10^{-5}$ s^{-1}), in this case the coupling is computed using Eq. (16.b). For multiplets from different branches with $\delta\omega_{KK'} > 10^{-5}$ s^{-1}, the coupling is computed normally according to Eqs. (16.c) and (16.d).

With this last precaution, a large number of overtones and also conversions between toroidal and spheroidal modes can be taken into account. The resulting perturbed seismogram takes into account all phases including body waves and surface waves. Similarly to the fundamental branch case, we must take care of ‘‘ghosts’’ for higher modes by coupling along branches and also between branches with a large enough Δl. However, even with large Δl, acausal ghosts do not totally vanish, and residual ghosts will mix with scattered body waves. Since acausal ghosts always arrive before the real perturbed phase, this can be avoided, if necessary, with judiciously placed Heaviside functions for each branch coupling, to reset this spurious signal.

An example of each level of approximation is given in Fig. 4, separating Rayleigh waves scattered into Rayleigh waves from Love waves scattered into Rayleigh waves. The plume is a ‘‘line plume’’ with temperature contrast $\Delta T = 400$ K (see relations (29)). The source-plume-receiver geometries are shown in the top of Fig. 4. In order to show incident Love wave scattered into Rayleigh wave, the scattered signals are not recorded in the alignment of the source and the plume, but at receiver 2. As a matter of fact, there is no incident Love wave scattered into Rayleigh wave in the forward direction (Bostock, 1991). This will be detailed in Section 4.2. In order to compare with the scattered signal, the incident signal is recorded at the same epicentral distance, at receiver 1. Besides, in this configuration, acausal ghosts arrive at $t = 0$ s (see Appendix C), and no mixing with real phases is possible. For scaling reasons, body waves (left panels) are separated from surface waves (right panels). All seismograms and scattered seismograms of Fig. 4 have been computed by using the first 60 overtones and the fundamental toroidal and spheroidal overtones in the period range between 40 and 200 s.

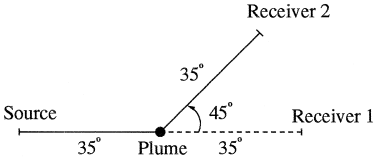

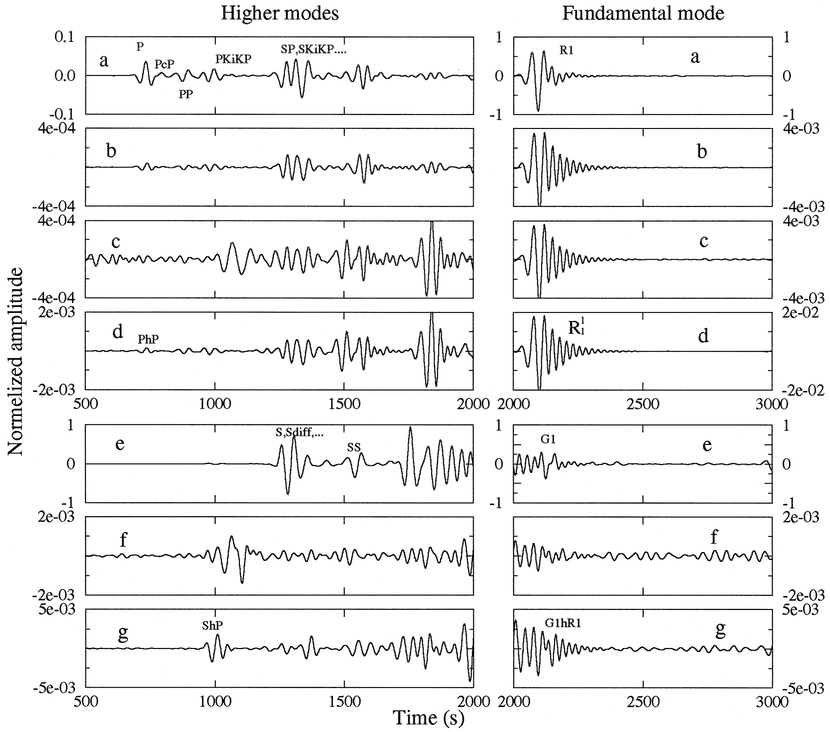

Fig. 4. (a) Vertical component of the incident signal, for the reference Earth model seismogram, recorded at the receiver 1, computed with (a) with the first 60 Rayleigh overtones with a period range of 40–200 s. (b) Vertical component of the scattered signal due to a ''line plume'' (see Section 3), recorded at receiver 2, in the isolated multiplet approximation, computed with (b). (c) Vertical component of the scattered signal recorded at receiver 2, coupling resonant multiplets from different Rayleigh overtones. The incident wave is the vertical component (a) only (no transverse component). (d) Vertical component scattered signal recorded at receiver 2, computed with (b), (c) and (d) (with $\Delta l = 60$) with only Rayleigh multiplets. The incident wave is the vertical component (a) only (no transverse component). (e) Transverse component of the incident signal, for the reference Earth model seismogram, recorded at the receiver 1, computed with (a) with the first 60 Love overtones with a period range of 40–200 s. (f) Vertical component of the scattered wave recorded at receiver 2, coupling resonant multiplets from different Love and Rayleigh overtones. The incident wave is the transverse component (e) only (no vertical component). (g) Fully coupled Love to Rayleigh multiplets scattering recorded at receiver 2, computed with (c) and (d), with $\Delta l = 60$. The incident wave is the transverse component (e) only (no vertical component). ShP is the S wave scattered into P wave by the plume and PhP the P wave scattered into P wave. The scattered signals (b), (c) and (d) are normalized with respect to the incident signals (plot a) and (f) and (g) with respect to (e). The left and the right part of the first four panels have different vertical scales. Note that waveform and amplitude are different between approximate and (nearly) fully coupled scattered seismograms.

Fig. 4a and e display, respectively, the vertical and the transverse component of the incident wave, recorded at receiver 1.

Fig. 4b, c and d show the vertical component of the scattered signal computed with different levels of approximation detailed below. In Fig. 4b to d, only the vertical component of the incoming wave have been used to compute the scattered signal, therefore, only Rayleigh waves scattered into Rayleigh waves and P waves scattered into P waves exist.

- Fig. 4b is computed in the isolated multiplet approximation.
- Fig. 4c is computed by coupling resonant multiplets from different Rayleigh overtones. A multiplet k_1 of a given branch n_1 is said to be resonant with a multiplet k_2 of a branch n_2 if k_2 makes $|\omega_{k1} - \omega_{k2}|$ minimum. k_2 is the ''nearest'' multiplet of n_2 to k_1 in the frequency domain. Note that if $n_1 = n_2$, then $k_1 = k_2$.
- Fig. 4d is computed by coupling all multiplets along and between Rayleigh branches up to $\Delta l = \pm 60$.

Fig. 4f and g also show the vertical component of the scattered signal computed with different levels of approximation detailed below. The difference with Fig. 4b, c and d is that only the transverse component of the incoming wave have been used to compute the scattered signal. Therefore, only Love waves scattered into Rayleigh waves and SH waves scattered into P waves exist.

- Fig. 4f is computed by coupling resonant multiplets from Love overtones with Rayleigh overtones.
- Fig. 4g is computed by coupling all Love multiplets with Rayleigh multiplets up to $\Delta l = \pm 60$.

In the isolated multiplets approximation (Fig. 4b), a wrong amplitude and a wrong waveform is obtained compared to the nearly fully coupled cases (Fig. 4d). When the coupling between resonant multiplets from different branches is taken into account (Fig. 4c and f) the waveform is correct except for the first arrivals, but the amplitude is wrong. Therefore it is important to take into account coupling between multiplets with a large enough Δl to obtain the right amplitude and waveform.

Note that the scattered signal on all body wave phases has been computed in Fig. 4d and g, in particular P wave scattered into P wave (phase PhP of Fig. 4d, ''h'' for heterogeneity) and S wave scattered into P wave (phase ShP of Fig. 4g). However, this complete computation involves a large number of interactions, and is quite time consuming on a workstation (about a day of CPU time).

4. Effect of different types of hotspots

The structure at depth of plumes is not well known, and some different assumptions can be made regarding their shape. In order to quantify the effect of different realistic plume structures, we test three simple geometries, shown in Fig. 5.

- Plume (1) corresponds to a cylinder of constant width from the D″ layer up to the surface.
- Plume (2) corresponds to a cylinder of constant width from the 670 km discontinuity up to the surface.
- Plume (3) corresponds to two cylinders of constant width, the first one from the D″ layer up to, for example, a depth of 100 km, and the second one, wider, from 100 km depth up to the surface, in order to simulate the head of the plume.

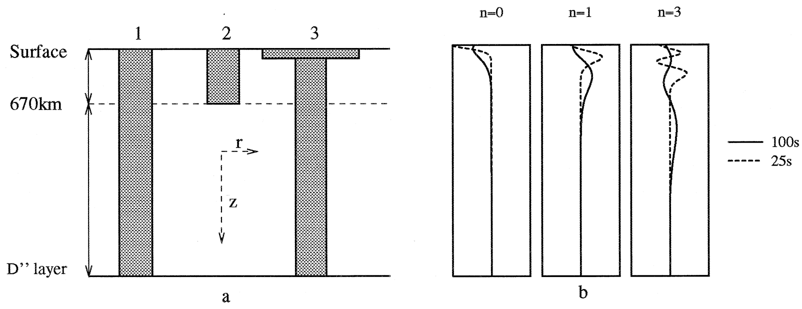

Fig. 5. (a) The three types of hotspot geometries tested in Section 4. (b) Spheroidal mode eigenfunctions, corresponding to vertical displacement, plotted for two periods, 25 s (dashed line) and 100 s (solid line), for $n = 0$, 1 and 3 at the same depth scale.

The temperature distribution within the plume has been choosen as follows (Farnetani, 1997):

$$\Delta T(r,z) = \Delta T_0 \exp\left[\frac{g\alpha}{c_p} z\right] \exp\left[-\left(\frac{r^2}{r_0^2}\right)\right] H(r_0 - r) \tag{28}$$

with the thermal expansion coefficient $\alpha = 2.10^{-5}$ K^{-1}, the specific heat at constant pressure $c_p = 1200$ J kg^{-1} K^{-1}, the gravity field $g = 10$ ms^{-2}. The orientation of r and z axes are shown in Fig. 5a, and r_0 is the radius of the plume. The density variation can be obtained with the following relation:

$$\frac{\delta_\rho}{\rho} = -\alpha \Delta T$$

and the corresponding seismic velocity contrast can be expressed by:

$$\frac{\delta v_p}{v_p} = \alpha_{\rho p}^{-1} \frac{\delta \rho}{\rho},$$

$$\frac{\delta v_s}{v_s} = \alpha_{sp} \frac{\delta v_p}{v_p}, \tag{29}$$

with $\alpha_{sp} = 1.25$ and $\alpha_{\rho p} = 0.5$ (Kumazawa and Anderson, 1969). The integration over the plume structure is performed according to Eq. (19) with a lateral sampling of at least five points per the shortest wavelength of the incident signal.

Since this work is done in the framework of the Born approximation, all multiple reflections and multiple scattering effects are neglected. The limitations of this approximation have been studied by Friederich et al. (1993) in the case of a cylinder with a constant velocity anomaly, in a flat Earth. They have shown that the effect of multiple forward scattering start to be significant, for a velocity contrast of 5%, when the ratio of the radius versus wavelength (r_0/λ) is between 1 and 2. In this paper, the obtained velocity contrasts have the same order of magnitude (between 1% and 10%) as in Friederich et al. (1993). For a period of 25 s, the wavelength of the fundamental mode is approximately 100 km, therefore the multiple scattering effect is negligible up to a radius of 100 km. In the case of a plume with a head of 200 km radius, the limit is reached. Even in this case, Friederich et al. (1993) have shown that the difference between the Born approximation (single scattering) and the multiple scattering modeling is only significant near the plume and is negligible at a distance of a few wavelengths. Therefore, the single scattering approximation is correct in the cases tested here. However, if this method is applied to larger heterogeneities (such as slabs for example) we should be careful of this limitation.

4.1. Spectra of scattered trains

The purpose of this section is to evaluate the influence of the different plume structures, shown in Fig. 5, on the amplitude spectra of the first scattered train. To this end, the spectra of the scattered signal are computed without cross-branch coupling, with an incident signal computed with only modes of a given branch. Fig. 6 (top) shows the spectrum of the incident wave, recorded at the receiver, computed with only the fundamental mode (a), or higher modes $n = 1$ (b) or 3 (c). Below are plotted the spectra of the corresponding scattered signals for each value of

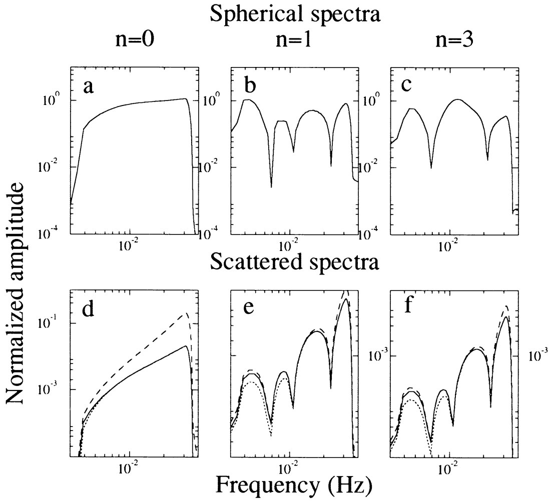

Fig. 6. Spectra as a function of the frequency for the same source and receiver location as in Section 2. The plume center is located at the middle of the source-receiver path and is represented by a distribution of points with a lateral sampling of, at least, five points per wavelength of the incident wave. Top: Spectra of the R1 Rayleigh train for the different overtone numbers, $n = 0$, $n = 1$ and $n = 3$. Bottom: Spectra, normalized by the corresponding incident signal spectrum, of the scattered signals of the R1 Rayleigh wave train computed coupling the incident overtone with itself: plume type 1 (solid line), plume type 2 (dotted line) and plume type 3 (dashed line).

n (Fig. 6d, e and f), computed coupling modes only along the same overtone. The three curves (solid line, dashed line and long dashed line) correspond to the three plume geometries showed in Fig. 5.

The difference between the spectra associated with plume of type 1 (solid line in Fig. 6) and 2 (dotted line) can only be observed at very low frequencies and is very weak for $n = 0$ but it is increasing with overtone number n. On the other hand, the difference between plume 3 and the two others is large and is more important at high frequency. This can be easily understood by considering the variation with depth of the eigenfunctions plotted in Fig. 5b, for $n = 0$, 1 and 3, with the same depth scale as the plumes. It shows that the difference between plume (1) and (2) is nearly impossible to detect in spectra of the fundamental mode only, even at long periods, because its sensitivity is concentrated near the surface, and is not able to ''see'' the lower mantle. Higher modes are better suited to discriminate between different plume models at depth because of their enhanced sensitivity there. The same interpretation explains the difference between spectra associated with plume 3 (dashed line) and those associated with the other plume models: the sensitivity of the modes is more concentrated near the surface when the frequency is high, and hence the modes are more sensitive to the plume head. Since the effect of the head is more important than that of the tail, it explains the strong difference at ''short'' periods and the little difference at very long periods, between plume (1) and plumes (2) and (3). In this case, the strong effect of the head on the fundamental mode hides the effect of the tail.

Fig. 6 also shows that, whatever the type of plume, high frequencies are more affected by the heterogeneity than low frequencies (compare, for example, the incident and the scattered spectra for $n = 0$).

The practical consequence of these observations is that a study using short period signals (around 30 s or less) is more interesting than one at very long periods (100 s or more) because the relative perturbed amplitude is the largest at short periods. In order to resolve plumes in the transition zone or in the lower mantle, we have to use periods longer than 100 s and also overtones. Therefore, by using the fundamental mode and the first higher modes, only the structure in the upper mantle can be retrieved. To resolve the very deep structure of the plume, higher modes of overtone numbering higher than 3 are required.

4.2. Radiation patterns

It is now interesting to determine if there is an optimum azimuth for detecting plumes. The ''radiation pattern'' of the heterogeneity is defined here as the ratio of the amplitude of the scattered signal with respect to the amplitude of the incident signal, at a given frequency, as a function of the scattering angle $\psi = \alpha_{sd} + \gamma_{dr}$ (Fig. 1). The source-plume-receiver geometry is described in (Fig. 7), the scattered signal is recorded at the station R(ψ) and compared to the incident signal recorded by the station N, located at the same epicentral distance as R(ψ). First we compute the radiation pattern when the heterogeneity is a ''line plume'' (see Section 4). We then investigate how the radiation pattern is modified by taking into account the lateral extent of the hotspot by a lateral integration. The numerical lateral integration is equivalent to consider that the plume is composed of a finite set of scattering points, and a summation over this set is performed (see Section 2). Here, only radiation patterns computed with the fundamental mode are discussed.

When the plume is assumed to be a vertical line of points (Fig. 8), spheroidal-to-spheroidal (equivalently Rayleigh-to-Rayleigh) radiation pattern has two lobes for the fundamental mode, and the most important one is in the forward direction. Toroidal-to-toroidal (equivalently Love-to-Love) has four lobes of equal amplitudes in forward, backward and lateral directions. Toroidal-to-spheroidal and spheroidal-to-toroidal (conversions) radiation patterns have two lateral lobes. Here we see again that scattering is stronger at high frequencies than at low frequencies. If the lateral extent of the heterogeneity

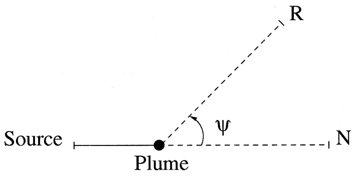

Fig. 7. Configuration used to construct ''Radiation patterns''.

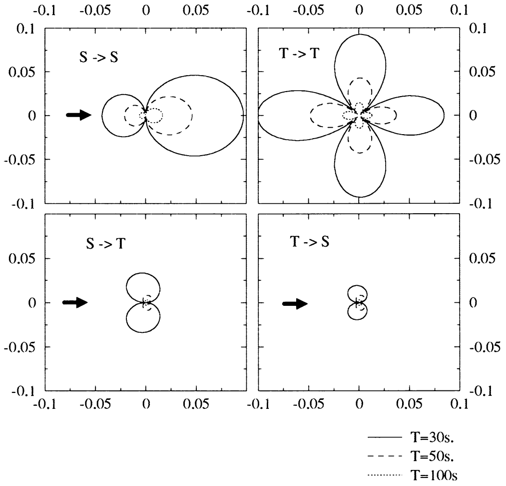

Fig. 8. Radiation patterns of the scattered wave amplitude with respect to the incident wave amplitude, in configuration of Fig. 7, for a vertical line of point heterogeneities for a radius of 100 km (plume type 1) and for the fundamental mode with $\Delta l = 30$. T refers to toroidal modes, S to spheroidal modes and for example, T → S refers to a conversion from toroidal to spheroidal modes. These ''radiation patterns'' are plotted for three periods, 30, 50 and 100 s. Black arrows indicate the incident wave direction.

is taken into account, the radiation patterns are greatly affected when the wavelength is smaller than three times the radius of the plume (Fig. 9). Most of the backward and lateral radiations vanish and the forward lobes become sharper. Even though the radiation patterns are largely dependent upon the lateral extent of the plume, for spheroidal-to-spheroidal scattering, the maximum effect on amplitude is still the same in the forward direction. For a radius of 100 km and an average temperature contrast of 400 K the maximum effect is about 10% of the incident amplitude at 30 s, 4% at 50 s and 2% at 100 s.

The influence of the extent of small heterogeneities on radiation patterns has been studied by Snieder (1986b) and Bostock (1991). Snieder (1986b), using an asymptotical formalism for a flat Earth, shows that this effect can be very large in the case of a mountain topography. For a constant velocity contrast cylinder and for a flat Earth, Bostock (1991) obtains the same effect on radiation patterns. Unfortunately, no scale was given in his figures and thus no further comparison is allowed. Note also that the shape of the radiation patterns of any small scale heterogeneity are always similar for the same ratio radius over wavelength. Little differences in the shape of radiation patterns which should be identical are often due to the fact that they are very sensitive to the relative composition of the heterogeneity in $\delta\mu/\mu$, $\delta\rho/\rho$ and $\delta\lambda/\lambda$ and then to the coefficients of Eq. (29).

Radiation patterns computed with overtones have also been studied and can display very complex shapes when considering a line plume, but when considering the lateral extent of the plume, only the forward scattering still remains.

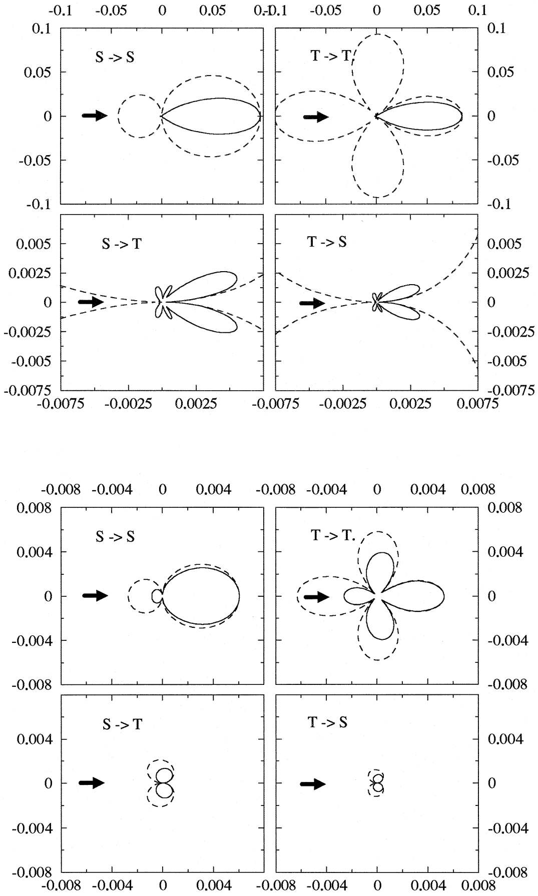

Fig. 9. Radiation patterns when the lateral extent of the plume is taken into account by a distribution of points, computed for the fundamental mode. Solid line: radiation patterns for a plume of type 1 with $r_0 = 100$ km on the top and $r_0 = 25$ km at the bottom, $T = 30$ s. For comparison radiation patterns of the same ''plume'', but represented by a vertical line of points, are plotted as dashed lines.

From the observational point of view, the effect of lateral extent is a problem. It would have been interesting to have energy scattered in another direction than the forward one. As a matter of fact, the time delay of a scattered wave compared to the direct signal is minimum in the forward direction and increases with the scattered azimuth (ψ in Fig. 7). When the direct and the scattered signals arrive at the same time, there is obviously a problem to extract it. We face the same problem when exploring the lower mantle: in the high frequency domain, the scattered energy is important but only in the forward direction, and it is mixed with the incident wave. At low frequencies, there is lateral and backward scattering but the amplitude is very weak. Therefore, the near alignment of the station, receiver and plume is the best configuration in which perturbed signal can be observed, if it can be separated from the direct signal and if there are no other structure that produces an equivalent scattering signal on the path.

5. Conclusions

The effect of different plume geometries have been computed in a 1-D spherical Earth model, using the Born approximation in the framework of normal mode theory. The use of the spherical harmonics summation theorem applied to generalized spherical harmonics allows the computation of perturbed seismograms, including a large number of interaction terms between modes. It is shown that it is very important to take into account the coupling between multiplets very far along branches to remove spurious phases and to obtain a correct amplitude. The method also allows the computation of the effect of a plume on all body wave phases, but it involves a very large number of modes, leading to an important numerical effort.

We show that the effect of a plume at ‘‘long periods’’ (more than 100 s) is different from the one at ‘‘short periods’’ (less than 100 s). The sensitivity at depth of surface waves decreases as the frequency increases. The low sensitivity of the fundamental mode at depth implies that only the shallow structure will be resolved by using it. Even with very long period data (more than 250 s), it will be impossible to discriminate a plume that comes from the D$''$ layer from one that originates from the transition zone (400–670 km). Of course it is possible to obtain deeper resolution using higher modes sensitive to larger depth than the fundamental modes. Nevertheless, most of the time, higher modes are, by far, less excited by earthquakes than the fundamental mode, and therefore it is more difficult to extract the corresponding scattered signal from data. Consequently the shallow structure is easier to retrieve from data. It is also shown that radiation patterns at ‘‘long’’ period and ‘‘short’’ period are different. If the ratio radius of the plume versus the shortest wavelength of the incident signal is small compared to 1, then the scattered energy can be observed in almost all directions, even backwards, and coupling between Rayleigh and Love modes are important. From a practical point of view, this case is quite interesting because, when the energy is scattered in directions other than the forward one, the scattered signal does not arrive at the same time as the direct signal, and is then easier to extract from data. If the plume radius is comparable to the wavelength, the scattered energy can only be observed in the forward direction, and there is no more coupling between Rayleigh and Love modes. For a radius of 100 km, this effect appears around a period of 100 s.

We also show that the ratio of the scattered amplitude to the incident amplitude is greater at ‘‘short’’ period than at ‘‘long’’ period: the scattered amplitude is about 10% of the incident amplitude at 30 s, 4% at 50 s and 2% at 100 s, for a plume radius of 100 km and an average temperature contrast of 400 K.

This shows that a compromise has to be found: on one hand, ‘‘long’’ periods are sensitive to deeper structure and energy is scattered in almost all directions but with a very weak amplitude. On the other hand, ‘‘short’’ periods have stronger scattered signal amplitude, but less sensitivity at depth and energy is scattered only in the forward direction. It turns out that the alignment of the plume, the station and the receiver is the configuration that provides the best chances to observe a scattered signal on seismograms. In this case, synthetic seismograms of the direct waves, that take into account all of the effects of different known structures along the path between the source and the receiver, are required to be able to extract the scattered signal from other signals. Since in this configuration an observable effect is only significant on the amplitude, a station close to the plume is necessary to well constrain the incident amplitude. If the plume effect is seen by this way, it will be necessary to use higher modes to study the deeper structure of the hotspot, and then earthquakes at different depths will be needed. In a complementary way, long period waves can also be studied to retrieve deeper structures. Of course, the scattered amplitude of long period surface wave is very weak, but it exists in almost all directions, which enables one to use a large number of data.

Finally, note that the plume effect on the amplitude varies as the square of its radius; if $r_0 = 50$ km instead of 100 km as in the previous example, the amplitude is divided by 4 which leads to an effect of 1% instead of 4% at 50 s. This means that our ability to detect the scattered signal on data is clearly related to the plume radius.

Such an application is attempted on the Hawaii hotspot (Stutzmann et al., 1997) where two GEOSCOPE stations, KIP and PPT, are particularly well located to study it. As a matter of fact, PPT, Hawaii and the Aleutians earthquakes are nearly aligned, and KIP is just before the supposed location of the plume when considering the Aleutians earthquakes. The numerical method presented in this paper will be used in order to test this application with synthetic seismograms.

Acknowledgements

We thank W. Friederich and F. Pollitz for critically reviewing the manuscript and making several useful remarks. Thanks to B. Romanowicz and E. Clévédé for helpful discussion. This is IPGP contribution 1575.

Appendix A. Expression of the matrix elements of $\rho_0^2 H^{-1}$

The purpose of this appendix is to show that

$$\left(\rho_0^2 \overline{H}^{-1}\right)_{kk'} = \langle \mathbf{k} | \rho_0^2 \overline{H}^{-1} | \mathbf{k}' \rangle = \delta_{kk'} / \left(\sigma_k^2 - \sigma^2\right). \tag{30}$$

We start from the fact that

$$H^{-1} H = I, \tag{31}$$

which, using the closure relation leads to

$$\sum_{k''} \rho_0 H^{-1} | \mathbf{k}'' \rangle \langle \mathbf{k}'' | H = I, \tag{32}$$

$$\sum_{k''} \langle \mathbf{k} | \rho_0^2 H^{-1} | \mathbf{k}'' \rangle \langle \mathbf{k}'' | H | \mathbf{k}' \rangle = \langle \mathbf{k} | \rho_0 | \mathbf{k}' \rangle. \tag{33}$$

Finally we use Eq. (5) to obtain

$$\langle \mathbf{k} | \rho_0^2 H^{-1} | \mathbf{k}' \rangle \left(\sigma_{k'}^2 - \sigma^2\right) = \delta_{kk'}, \tag{34}$$

$$\langle \mathbf{k} | \rho_0^2 H^{-1} | \mathbf{k}' \rangle = \frac{\delta_{kk'}}{\left(\sigma_k^2 - \sigma^2\right)}, \tag{35}$$

which is the wanted result.

Appendix B. Expressions of $\delta A_{KK'N}$ and $\delta P_{KK'N}$ matrix elements

$$\langle \mathbf{k} | \delta A | \mathbf{k}' \rangle = \sum_{ijpq} \int_E {}_k u_i^* \frac{\partial}{\partial x_j} \left\{ \delta c_{ijpq}(\mathbf{x}) \frac{\partial_{k'} u_p}{\partial x_q} \right\} \mathrm{d}^3 x, \tag{36}$$

where δc is the perturbation to the elastic tensor and ${}_k\mathbf{u}$ is the displacement associated to the mode $|\mathbf{k}\rangle$. For a point heterogeneity, using an integration by part and the symmetry of the elastic tensor, we have,

$$\delta A_{kk'} = -\sum_{ijpq} \int_E {}_k \mathrm{e}_{ij}^* \left\{ \delta c_{ijpq} \delta(\mathbf{x} - \mathbf{x}_d)_{k'} \mathrm{e}_{pq} \right\} \mathrm{d}^3 x, \tag{37}$$

$$\delta A_{kk'} = -\sum_{ijpq} \delta c_{ijpqk} \mathrm{e}_{pq}^* (\mathbf{x}_d)_{k'} \mathrm{e}_{pq}(\mathbf{x}_d), \tag{38}$$

where ${}_k\mathrm{e}_{ij} = 1/2((\partial_k u_i)/(\partial x_j) + (\partial_k u_j)/(\partial x_i))$ is the strain tensor. In the isotropic case $c_{ijpq} = \lambda \delta_{ij}\, \delta_{pq} + \mu(\delta_{ip}\delta_{jq} + \delta_{iq}\delta_{jp})$, then:

$$\begin{aligned} \delta A_{kk'} = & -\delta\lambda \left(\sum_i {}_k \mathrm{e}_{ii}^* (\mathbf{x}_d) \right) \left(\sum_p {}_{k'} \mathrm{e}_{pp}(\mathbf{x}_d) \right) \\ & -2\delta\mu \left(\sum_{pq} {}_k \mathrm{e}_{pq}^* (\mathbf{x}_d)_{k'} \mathrm{e}_{pq}(\mathbf{x}_d) \right). \end{aligned} \tag{39}$$

As for $\delta\rho$:

$$\delta P_{kk'} = \delta\rho \sum_i {}_k u_i^* (\mathbf{x}_d)_{k'} u_i(\mathbf{x}_d). \tag{40}$$

These matrix elements can be computed on the generalized spherical harmonics basis of Phinney and Burridge (1973) (see Eqs. (24) and (25)). Keeping their notations and following for example Tanimoto (1986) we find:

$$\begin{aligned}
\delta A_{KK'\pm 2} &= -8\delta\mu \frac{k_2^l k_2^{l'}}{r_d^2} (V_K \mp iW_K)(V_{K'} \pm iW_{K'}), \\
\delta A_{KK'\pm 1} &= -2\delta\mu k_1^l k_1^{l'} (X_K \mp iZ_K)(X_{K'} \pm iZ_{K'}), \\
\delta A_{KK'0} &= -\delta\lambda\, k_0^l k_0^{l'} \left(\frac{\mathrm{d}U_K}{\mathrm{d}r} + F_K \right) \left(\frac{\mathrm{d}U_{K'}}{\mathrm{d}r} + F_{K'} \right) \\
&\quad - \delta\mu\, k_0^l k_0^{l'} \left(F_K F_{K'} + 2 \frac{\mathrm{d}U_K}{\mathrm{d}r} \frac{\mathrm{d}U_{K'}}{\mathrm{d}r} \right),
\end{aligned} \tag{41}$$

$$\begin{aligned}
\delta P_{KK'\pm 1} &= 2\delta\rho k_1^l k_1^{l'} (V_K \mp iW_K)(V_{K'} \pm iW_{K'}), \\
\delta P_{KK'0} &= \delta\rho k_0^l k_0^{l'} U_K U_{K'},
\end{aligned} \tag{42}$$

where ${}_nU_l$, ${}_nV_l$ and ${}_nW_l$ are the radial eigenfunctions, ${}_nU_l = {}_nV_l = 0$ for a toroidal mode and ${}_nW_l = 0$ for a spheroidal one, $\Omega_{\mathrm{N}}^l = (((l+N)(l-N+1))/2)^{1/2}$, $\gamma_l = ((2l+1)/(4\pi))^{1/2}$, $k_0^l = \gamma^l$, $k_1^l = (1/\sqrt{2})\gamma^l \Omega_0^l$, $k_2^l = \Omega_2^l \Omega_0^l \gamma^l/2$ and finally

$$F_K = \frac{(2U_K - l(l+1)V_K)}{r}, \tag{43}$$

$$Z_K = \frac{\mathrm{d}W_K}{\mathrm{d}r} - \frac{W_K}{r}, \tag{44}$$

$$X_K = \frac{\mathrm{d}V_K}{\mathrm{d}r} + \frac{(U_K - V_K)}{r}. \tag{45}$$

All eigenfunctions and their derivatives are taken at the radius of the scattered point, r_d.

Appendix C. ‘‘Ghost’’ trains

In this appendix we show that ‘‘ghost’’ trains are a consequence of the ‘‘isolated multiplet’’ approximation. To do so, asymptotic expressions of the spherical harmonics are used. The Poisson formula enables one to convert the mode summation into a propagating waves form in which ‘‘Ghosts’’ appear more clearly. For sake of simplicity let us consider a point heterogeneity in $\delta\lambda$ such that $\delta H_{KK'N''} = \delta H_{KK'0}\delta_{N'',0}$. In this case:

$$\begin{aligned}
\sum_{mm'} R_K^m S_{K'}^{m'} \delta H_{KK'}^{mm'} &= \sum_{NN'} R_{KN} S_{K'N'} \mathrm{e}^{i(N'\gamma_{sd} + N\alpha_{dr})} \\
&\quad \times \delta H_{KK'0} . P_{l'}^{N'}(\cos(\beta_{sd})) \\
&\quad \times P_l^N(\cos(\beta_{dr})).
\end{aligned} \tag{46}$$

Let us define $J_{KK'} = \sum_{mm'} R_K^m S_{K'}^{m'} \delta H_{KK'}^{mm'}$.

For $l \gg 1$ Legendre functions may be expressed asymptotically (Robin, 1958),

$$\begin{aligned}
P_{l'}^N(\cos(\beta)) &= \sqrt{\frac{2\pi}{(l+1/2)}} \frac{1}{\pi\sqrt{\sin\beta}} \\
&\quad \times \cos\left((l+1/2)\beta - \frac{\pi}{4} + \frac{N}{2}\pi \right),
\end{aligned} \tag{47}$$

thus

$$\begin{aligned}
J_{KK'} &= \sum_{NN'} 2 I_{KK'}^{NN'} \cos\left((l'+1/2)\beta_{sd} - \frac{\pi}{4} + \frac{N'}{2}\pi \right) \\
&\quad \times \cos\left((l+1/2)\beta_{dr} - \frac{\pi}{4} + \frac{N}{2}\pi \right),
\end{aligned} \tag{48}$$

where

$$I_{KK'}^{NN'} = \frac{R_{KN} S_{K'N'} \mathrm{e}^{i(N'\gamma_{sd} + N\alpha_{dr})} \delta H_{KK'0}}{\pi\sqrt{(l+1/2)(l'+1/2)\sin(\beta_{sd})\sin(\beta_{dr})}}. \tag{49}$$

In the isolated multiplet approximation, $K = K'$, the expression of the scattered signal $\delta\mathbf{u}$ to $\mathbf{u}$ is

$$\begin{aligned}
\delta\mathbf{u}.\mathbf{v} &= \sum_l J_{KK} \cos(\sigma_K t) \\
&= \sum_{l=0}^{\infty} \sum_{NN'} I_{KK}^{NN'} \cos(\sigma_K t) \\
&\quad \times \left[\cos((l+1/2)\theta_1 + \phi_1) \right. \\
&\quad \left. + \cos((l+1/2)\theta_2 + \phi_2) \right],
\end{aligned} \tag{50}$$

with $\theta_1 = \beta_{sd} + \beta_{dr}$, $\theta_2 = \beta_{sd} - \beta_{dr}$, $\phi_1 = (N + N' - 1)/\pi/2$ and $\phi_2 = (N - N')/\pi/2$. If we now define

- ${}^1I^{NN'}_{s,n,l} = I^{NN'}_{s,n,l}\mathrm{e}^{i\phi_1}$ for $l \geq 0$,
- ${}^1I^{NN'}_{s,n,l} = I^{NN'}_{s,n,-l-1}\mathrm{e}^{-i\phi_1}$ for $l < 0$,

and similarly define ${}^2I^{NN'}_K$ with ϕ_2 instead of ϕ_1, Eq. (50) can be rewritten

$$\delta\mathbf{u}.\mathbf{v} = \sum_{l=-\infty}^{\infty} \sum_{NN'} \cos(\sigma_K t)\Big[{}^1I^{NN'}_K \mathrm{e}^{i(l+1/2)\theta_1} + {}^2I^{NN'}_K \mathrm{e}^{i(l+1/2)\theta_2}\Big]. \tag{51}$$

The Poisson sum formula can then be used to obtain:

$$\begin{aligned}\delta\mathbf{u}.\mathbf{v} = \sum_{NN'} \sum_{q=0}^{\infty} \int_{-\infty}^{+\infty} \mathrm{d}\nu (-1)^q \sum_{\epsilon=\pm 1} & \times\Big[{}^1I^{NN'}_{\nu}\big(\mathrm{e}^{i(\epsilon\sigma_K t + \nu(\theta_1 - 2\pi q))} \\ & + \mathrm{e}^{i(\epsilon\sigma_K t + \nu(\theta_1 + 2\pi(q+1)))}\big) \\ & + {}^2I^{NN'}_{\nu}\big(\mathrm{e}^{i(\epsilon\sigma_K t + \nu(\theta_2 - 2\pi q))} \\ & + \mathrm{e}^{i(\epsilon\sigma_K t + \nu(\theta_2 + 2\pi(q+1)))}\big)\Big],\end{aligned} \tag{52}$$

with $\sigma_K = \sigma_{s,n,\nu-1/2}$. Besides $\sigma_K \simeq \nu c/a$ (Snieder and Nolet, 1987), where a is the Earth's radius and c the phase velocity. Then eight phases are obtained for each q in which only the ones with a positive time arrival are considered:

$$t \simeq \pm\frac{a}{c}(\theta_1 - 2q\pi),$$

$$t \simeq \pm\frac{a}{c}(\theta_1 + 2(q+1)\pi),$$

$$t \simeq \pm\frac{a}{c}(\theta_2 - 2q\pi),$$

$$t \simeq \pm\frac{a}{c}(\theta_2 + 2(q+1)\pi).$$

For $q = 0$ two phases, which should not come up, appears. In the example of Fig. 2 they correspond to $t \simeq (a/c)\theta_2$ ($gh1$ in Fig. 2) and $t \simeq (a/c)(\theta_1 + \pi)$ ($gh2$ in Fig. 2).

References

Bostock, M.G., 1991. Surface wave scattering from 3-D obstacles. Geophys. J. Int. 104, 351–370.

Cazenave, A., Souriau, A., Dominh, K., 1989. Global coupling of Earth surface topography with hotspots, geoid and mantle heterogeneities. Nature 340, 54–57.

Clévédé, E., 1991. Modes Propres d'une Terre Sphérique Anélastique. Rapport de stage de DEA. IPGP.

Clévédé, E., Logonnné, P., 1996. Fréchet derivatives of coupled seismograms with an anelastic rotating Earth. Geophys. J. Int. 124, 456–482.

Cohen-Tannoudji, C., Diu, B., Laloë, F., 1977. Mécanique Quantique. Hermann, Paris, and Wiley, New York.

Dziewonski, A.M., Anderson, D.L., 1981. Preliminary reference Earth model. Phys. Earth Planet. Inter. 25, 297–356.

Edmonds, A.R., 1960. Angular Momentum and Quantum Mechanics. Princeton Univ. Press, NJ.

Farnetani, C.G., 1997. Excess temperature of mantle plumes: the role of chemical stratification across D″. Geophys. Res. Lett. 24, 1583–1586.

Farnetani, C.G., Richards, M.A., 1995. Thermal entrainment and melting in mantle plumes. Earth Planet. Sci. Lett. 136, 251–267.

Friederich, W., Wielandt, E., Stange, S., 1993. Multiple forward scattering of surface waves: comparison with an exact solution on Born single-scattering methods. Geophys. J. Int. 112, 264–275.

Grand, S., Van Der Hilst, R., Widiyantoro, S., 1997. Global seismic tomography: a snapshot of convection in the Earth. Geol. Soc. Am. Today 7 (4), 1–7.

Griffiths, R.W., Campell, I.H., 1990. Stirring and structure in mantle starting plumes. Earth Planet. Sci. Lett. 99, 66–78.

Hart, S.R., Hauri, E.H., Oschmann, L.A., Whitehead, J.A., 1992. Mantle plumes and entrainment: isotopic evidence. Science 256, 517–520.

Hofmann, A.W., 1997. Mantle geochemistry: the message from oceanic volcanism. Nature 385, 219–229.

Kumazawa, M., Anderson, O.L., 1969. Elastic moduli, pressure derivates, and temperature derivates of singe-crystal olivine and single-crystal forstite. J. Geophys. Res. 74, 5961–5972.

Li, X., Tanimoto, T., 1993. Waveforms of long-period body waves in slightly aspherical Earth model. Geophys. J. Int. 112, 92–102.

Lognonné, P., Clévédé, E., 1997. Diffraction of long period Rayleigh waves by a slab: effects of mode coupling. Geophys. Res. Lett. 24, 1035–1038.

Malischewsky, P., 1987. Surface Waves and Discontinuities. Elsevier, Amsterdam.

Minster, J.B., Jordan, T.H., 1978. Present-day plate motion. J. Geophys. Res. 83, 5331–5354.

Montagner, J.P., 1994. What can seismology tell us about mantle convection? Rev. Geophys. 32 (2), 115–137.

Montagner, J.P., 1996. Surface waves on a global scale — influence of anisotropy and anelasticity. In: Boschi, Ekstrom, and Morelli (Eds.), Summer School of Erice, Seismic Modeling of the Earth's Structure, pp. 81–148.

Montagner, J.P., Romanowicz, B., 1993. Degrees 2, 4, 6 inferred from seismic tomography. Geophys. Res. Lett. 20, 631–634.

Morgan, W., 1971. Convection plumes in the lower mantle. Nature 230, 42–43.

Nataf, H.C., Vandecar, T., 1993. Seismological detection of mantle plume? Nature 364, 115–120.

Olson, P., Scubert, G., Snderson, C., 1987. Plume formation in the D′ layer and the roughness of the core–mantle boundary. Nature 327, 409–413.

Phinney, R.A., Burridge, R., 1973. Representation of elastic-gravitational excitation of a spherical Earth model by generalized spherical harmonics. Geophys. J. R. Astron. Soc. 34, 278–451.

Robin, L., 1958. Fonctions Sphériques de Legendre et Fonctions Sphéroidales. Gauthier Villars, Paris.

Romanowicz, B., 1987. Multiplet–multiplet coupling due to lateral heterogeneity: asymptotic effects on the amplitude and frequency of the Earth's normal modes. Geophys. J. R. Astron. Soc. 90, 75–100.

Roult, G., Rouland, D., Montagner, J.P., 1994. Antarctica II: upper-mantle structure from velocities and anisotropy. Phys. Earth Planet. Inter. 84, 33–57.

Silveira, G., Stutzmann, E., Griot, D., Montagner, J.P., Mendes-Victor, L., 1998. Anisotropic tomography of the Atlantic Ocean from Rayleigh surface waves. Phys. Earth Planet. Inter. 106 (3–4), 259–275.

Snieder, R., 1986a. 3D Linearized scattering of surface waves and formalism for surface wave holography. Geophys. J. R. Astron. Soc. 84, 581–605.

Snieder, R., 1986b. The influence of topography on the propagation and scattering of surface waves. Phys. Earth Planet. Inter. 44, 226–241.

Snieder, R., Nolet, G., 1987. Linearized scattering waves on a spherical Earth. J. Geophys. 61, 55–63.

Stacey, F.D., Loper, D.E., 1983. The thermal boundary layer interpretation of D″ and its role to plume sources. Phys. Earth Planet. Inter. 33, 45–55.

Stange, S., Friederich, W., 1992. Guided wave propagation across sharp lateral heterogeneities: the complete wavefield at a cylindrical inclusion. Geophys. J. Int. 111, 470–482.

Stutzmann, E., Capdeville, Y., Montagner, J.P., 1997. Study of Hawaii Hotspot Structure Using Seismic Surface Waves. IASPEI 1997, Thessaloniki, Greece, Abstracts, pp. 241.

Tanimoto, T., 1984a. A simple derivation of the formula to calculate synthetic long period seismograms in heterogeneous Earth by normal mode summation. Geophys. J. R. Astron. Soc. 77, 275–278.

Tanimoto, T., 1984b. Waveform inversion of mantle love waves: the born seismogram approach. Geophys. J. R. Astron. Soc. 78, 641–660.

Tanimoto, T., 1986. Free oscillations of a slightly anisotropic Earth. Geophys. J. R. Astron. Soc. 87, 493–517.

Trampert, J., Woodhouse, J.H., 1995. Global phase velocity maps of Love and Rayleigh waves between 40 and 150 seconds. Geophys. J. Int. 122, 675–690.

Van Der Hilst, R., Widiyantoro, S., Engdahl, E., 1997. Evidence for deep mantle circulation from global tomography. Nature 386, 578–584.

Vinnik, L., Chevrot, S., Montagner, J.P., 1997. Evidence for a stagnant plume in the transition zone? Geophys. Res. Lett. 24, 1007–1010.

Whitehead, J.A., Luther, D.S., 1975. Dynamics of laboratory diapir and plume models. J. Geophys. Res. 80, 705–717.

Wolfe, C.J., Bjarnason, I.T., VanDecar, J.C., Solomon, S.C., 1997. Seismic structure of the Iceland mantle plume. Nature 385, 245–247.

Woodhouse, J.H., Dahlen, F.A., 1978. The effect of a general aspherical perturbation on the free oscillations of the Earth. Geophys. J. R. Astron. Soc. 53, 335–354.

Woodhouse, J.H., Girnius, T.P., 1982. Surface waves and free oscillations in a regionalized Earth model. Geophys. J. R. Astron. Soc. 78, 641–660.

Ying, J., 1996. Tomographie par Diffraction et Détection de Panaches Mantelliques dans le Manteau Inférieur. Thèse de doctorat de l'Université Paris 7.

Ying, J., Nataf, H.C., 1998. Detection of mantle plumes in the lower mantle by diffraction tomography: theory. Phys. Earth Planet. Inter. 159, 87–98.

Zhang, Y., Tanimoto, T., 1993. High-resolution global upper mantle structure and plate tectonics. J. Geophys. Res. 98, 9793–9823.